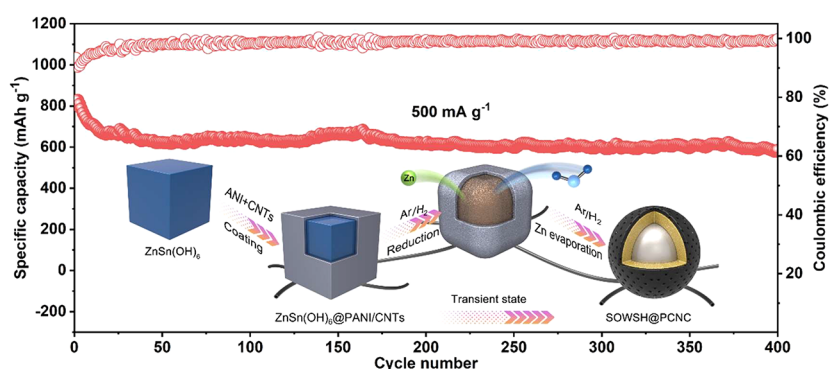# Interfacial Modulation of a Self-Sacrificial Synthesized SnO$_2$@Sn Core−Shell Heterostructure Anode toward High-Capacity Reversible Li$^+$ Storage

Bo Deng, Rong He, Jing Zhang,* Caiyin You, Yonglan Xi,* Qingbo Xiao, Yongzheng Zhang, Haitao Liu, Meinan Liu, Fangmin Ye,* Hongzhen Lin,* and Jian Wang*

ABSTRACT: Sn-based anodes are promising high-capacity anode materials for low-cost lithium ion batteries. Unfortunately, their development is generally restricted by rapid capacity fading resulting from large volume expansion and the corresponding structural failure of the solid electrolyte interphase (SEI) during the lithiation/delithiation process. Herein, heterostructural core−shell SnO$_2$-layer-wrapped Sn nanoparticles embedded in a porous conductive nitrogen-doped carbon (SOWSH@PCNC) are proposed. In this design, the self-sacrificial Zn template from the precursors is used as the pore former, and the LiF-Li$_3$N-rich SEI modulation layer is motivated to average uniform Li$^+$ flux against local excessive lithiation. Meanwhile, both the chemically active nitrogen sites and the heterojunction interfaces within SnO$_2$@Sn are implanted as electronic/ionic promoters to facilitate fast reaction kinetics. Consequently, the as-converted SOWSH@PCNC electrodes demonstrate a significantly boosted Li$^+$ capacity of 961 mA h g^{-1} at 200 mA g^{-1} and excellent cycling stability with a low capacity decaying rate of 0.071% after 400 cycles at 500 mA g^{-1}, suggesting their great promise as an anode material in high-performance lithium ion batteries.

INTRODUCTION

With the ever-increasing energy demands for portable mobile devices, electronic vehicles (EVs), and smart grids, the development of reversible systems as power sources with the merits of high energy density, great stability, and security is urgently needed.[1−6] Among diverse systems, secondary lithium ion batteries (LIBs) composed of various intercalated cathodes and a graphite anode gradually bloom their way to practical applications.[7−11] Unfortunately, the output of LIBs touches the bottleneck owing to the limited theoretical capacity of the graphite-based anode (372 mA h g^{-1}).[12−15] More effort has been devoted to seeking and developing alternative high-capacity anodes, such as metal alloys, metal oxides/sulfides, silicon, and their derivatives.[16−20] In particular, the Sn anode shows the advantages of high theoretical capacity (992 mA h g^{-1}) based on the alloying mechanism with Li$^+$ to form the maximum Li$_{4.4}$Sn, abundant resources, low cost, and high safety.[16,21−24] However, the tough obstacles in Sn anodes prevent further commercialization: (1) the huge volumetric variation of around 300% during lithiation/delithiation, resulting in the possible detachment from the electrode or the loss of electrical contact between active materials and the conductive matrix; (2) the repeated cracking and formation of a fragile solid electrolyte interphase (SEI) layer, causing the depletion of the finite electrolyte; and (3) the collapse and detachment of conductive Sn from the matrix, inducing the hardness of effective electronic transfer. These interconnected dissatisfactory factors contribute to the depressive capacity,
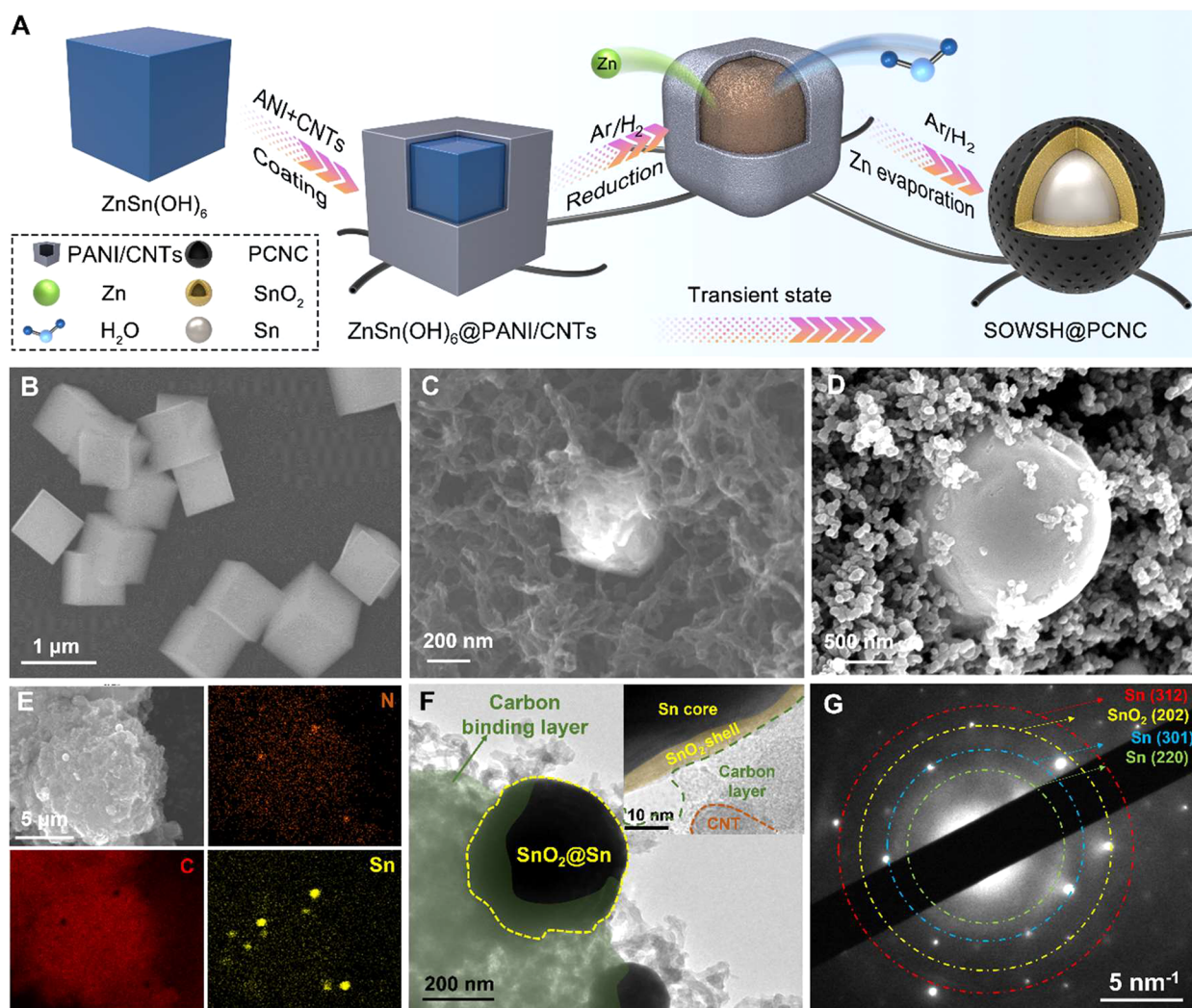
Figure 1. Schematic synthesis illustration and morphology characteristics of the SOWSH@PCNC nanocomposite. (A) Schematic illustration of the synthesis process of the SOWSH@PCNC nanocomposite. SEM images of (B) the $ZnSn(OH)_6$ precursor and (C) SOWSH@PCNC and (D) SOS@SP samples. (E) SEM energy-dispersive X-ray spectroscopy (EDS) elemental mapping of C, N, and Sn obtained in the SOWSH@PCNC. (F) Low-resolution TEM image. (G) Selected-area electron diffraction pattern of the SOWSH@PCNC nanocomposite.

cycling durance, and even battery failure in practical applications.[25−28]

Until now, diverse attempts have been put forward to tackle the aforementioned issues around improving the electro-chemical behaviors and capacity retention of the Sn electrode.[29−41] These strategies can be mainly classified into three aspects: (i) building electron-conductive network hosts to embed Sn;[16,32,33,35] (ii) constructing porous structure (i.e., metal−organic frameworks (MOFs)) to accommodate Sn particles and tolerate the severe volumetric changes;[26,36] and (iii) adopting the compatible electrolyte to generate the robust SEI layer to make the lithium ion flux uniform with respect to averaging the focused stress.[38,42−49] Although such effort can partially improve the utilization of active Sn species and the electrochemical performance in LIBs at the beginning, these simple stacked porous carbons not only merely provide transient physical barriers with poor mechanical stability against volumetric changes but also experience sluggish ion diffusion due to the lack of ion accelerators.

SnO_2, an n-type semiconductor with a wide band gap of 3.62 eV, is also an Sn-derived anode material based on the reaction of $SnO_2 + 4Li^+ \rightarrow Sn + 2Li_2O$.[30,34] The self-generated Li_2O on

the Sn surface would supply a buffer layer in the matrix and enhance an extended stable cycling stability.[32,34] In this regard, chemically compositing SnO_2 on the Sn surface seems to be of significance to maintain high performance. Various synthetic methods of synthesizing Sn-SnO_2 by oxygen plasma etching, the microwave plasma-assisted method, the solution-based method, and calcination are proposed.[30,50] However, the relatively complex synthesis method and strictly controlled conditions restrict their large-scale applications.[16,29] Therefore, a simple way to large-scale produce a Sn-SnO_2 heterostructure endowed with the desired electronic/ionic conductivity and strong compactness with robust mechanical integrity is a favorable alternative to ensure electrochemical reversibility of the Sn anode.

Herein, different from tedious synthesis, the SnO_2-wrapped Sn core−shell heterostructure embedded in porous and conductive nitrogen-doped carbon networks (SOWSH@PCNC) is proposed via a self-sacrificial template and *in situ* chemical transformation under a reductive atmosphere, as schematically illustrated in Figure 1A. In this approach, the highly conductive carbon nanotubes (CNTs) were self-assembled to build the highly conductive skeleton while

using the carbonized nitrogen-doped layer from a polymer as a "binder" to reinforce the mechanical integrity, further facilitating the pathway of electrons. The $ZnSn(OH)_6$ microcube precursors as self-sacrificial templates are decomposed to form Zn vapor and SnO_2-wrapped Sn core–shell ($SnO_2@Sn$) nanoparticles that are uniformly incorporated into the network. By the evaporation and sacrifice of Zn, abundant interspaces remained as volumetric buffers and affluent $SnO_2@Sn$ heterostructures were bred. Such unified structure endows the hybrid with robust tolerance to the volumetric changes. At the same time, the implanting of chemically active N sites and the constructed heterostructural $SnO_2@Sn$ layer as electronic/ionic promoters enable fast electron/ion transformation between the core skeleton and the Sn domains, providing fast reaction kinetics. On the other hand, a robust LiF-Li_3N-rich SEI layer on the surface of the $SnO_2@Sn$ electrode decomposed from the active LiTFSI is formed, as confirmed by electronic microscopes and X-ray photoelectron spectroscopy tests. Thanks to the double reinforcements from the formed robust LiF-Li_3N-rich SEI layer to the heterostructure layer of SnO_2 on the surface of Sn, our structure affords an effective modulation of lithium ion diffusion kinetics to average the lithium ion flux, avoiding focused stress. Consequently, the fabricated SOWSH@PCNC electrode displays remarkably enhanced lithium storage capacity with improved cycling stability and rate performance in comparison to that without a reinforced conductive skeleton and chemically active sites as electronic/ionic accelerators.

EXPERIMENTAL SECTION

Synthesis of the SOWSH@PCNC Nanocomposite. First, a $ZnSn(OH)_6$ template precursor was synthesized by fully dissolving $ZnCl_2$ (136 mg), poly(vinylpyrrolidone) (PVP, 100 mg), and $SnCl_4\cdot 5H_2O$ (351 mg) in 40 mL of deionized water, and then a 1 mol L^{-1} NaOH solution was added dropwise to the aforementioned solution with continuous magnetic stirring for 30 min. The obtained suspension was transferred to a hydrothermal reactor and placed in an oven kept at a constant temperature of 100 °C for 8 h. The resultant $ZnSn(OH)_6$ was collected by filtration and washed repeatedly until reaching pH 7.

Then, the above synthesized $ZnSn(OH)_6$ and 37.5 mg of CNTs with PVP (50 mg) were added to 200 mL of deionized water and dispersed by sonication for 2 h. A solution of 192 μL of aniline in 0.2 mol L^{-1} HCl was added to the dispersion with another sonication for 30 min before 100 mL of an ammonium persulfate (1.473 mg) aqueous solution was added dropwise with vigorous stirring under an ice bath and a flow of nitrogen. After stirring for 24 h, the composites were collected, washed repeatedly with deionized water, and finally freeze-dried for 24 h, yielding the precursor composites. After annealing at 900 °C at a heating rate of 5 °C min^{-1} under an Ar/H_2 (5%:95% by volume) atmosphere for 2 h to fully evaporate metallic Zn, the SOWSH@PCNC nanocomposite was finally obtained. For comparison, $ZnSn(OH)_6$ with commercial superconductive carbon black without robust interconnected structures was mixed and annealed at 900 °C under a reducing atmosphere to prepare the controlled SnO_2-Sn with a superconductive carbon composite (denoted as SOS@SP).

Preparation of Electrodes and Assembly of Coin Cells. First, the slurry was prepared by mixing the as-prepared SOWSH@PCNC nanocomposite, carbon black (Super P), and polyvinylidene fluoride (PVDF) with a mass ratio of 8:1:1 in N-methyl-2-pyrrolidone (NMP) solution with continuous stirring. Then, the uniform slurry was coated on a copper current collector with a film spreader to form a uniform layer. After vacuum drying at 60 °C for 48 h, the working electrode was punched into discs (11 mm in diameter) with an average weight loading of 1.2 mg cm^{-2}. The as-designed 2025-type coin cells were assembled with SOWSH@PCNC as the working electrode, Celgard 2400 as the separator, and metallic Li foil as the counter electrode. The LiTFSI (1 mol L^{-1}) with 1 wt % $LiNO_3$ dissolved in a mixed solvent of DME/DOL (v:v = 1:1) was adopted as the electrolyte. Briefly, the DME and DOL solvents were first mixed together in a volume ratio of 1:1. Then, 14.35 g of LiTFSI (1 mol L^{-1}) salt was dissolved in 50 mL of the DME/DOL mixed solvent to form a uniform solution by continuous stirring. Afterward, the specific amount of $LiNO_3$ was added to the above-formed LiTFSI solution based on a weight percentage of 1 wt %. A dosage of 15 μL mg^{-1} was dropped in each cell before assembling.

Material and Device Characterization. The X-ray diffraction (XRD) patterns were collected on an XRD-7000S X-ray diffractometer using Cu Kα radiation in the 2θ range from 10 to 80°. Scanning electron microscopy (SEM) and transmission electron microscopy (TEM) on the nanocomposites or cycled electrode were carried out by using a Germany MERLIN compact scanning electron microscope (Zeiss Sigma HD) and a JEOL JEM-3010 transmission electron microscope, respectively. The X-ray photoelectron spectra (XPS) were collected from an ESCALAB 250XI system to investigate the chemical surroundings of the different elements in the nanocomposites.

The galvanostatic tests were performed on a Neware Battery Testing System (BTS-5 V 20 mA) at various current rates within the voltage window of 0−3.0 V. Electrochemical impedance spectroscopy (EIS) was performed on an American Versa STAT 3F potentiostat/galvanostat station with a frequency range of 10^{-2} to 10^5 Hz. And cyclic voltammetry (CV) was tested within the voltage range of 0−2 V with a sweep rate of 0.02 mV s^{-1}.

RESULTS AND DISCUSSION

Guided by the above proposed design, the SOWSH@PCNC nanocomposite was synthesized by combining the hydrogen reduction with Zn (self-sacrificial template) evaporation treatment, as depicted in Figure 1A. Briefly, the highly conductive CNTs were assembled with the aid of the polyaniline (PANI) to form a highly conductive framework, which was further annealed under a reducing atmosphere (Ar/H_2) to transform PANI to the nitrogen-doped carbon layer as a "binding" reagent. At the same time, the self-sacrificial template was removed to form uniformly embedded SnO_2-wrapped Sn core−shell ($SnO_2@Sn$) nanoparticles in the porous and conductive nitrogen-doped carbon networks (SOWSH@PCNC). Owing to the existence of surface tension, the generated Sn and SnO_2 experience a reconstruction state from melting to solidification to reduce the surface tension, forming a sphere-like $SnO_2@Sn$ core−shell structure. For detailed verification, structure and morphology characteristics of the as-synthesized SOWSH@PCNC were then determined fully. Scanning electron microscopy (SEM) and transmission electron microscopy (TEM) were initially applied to observe the morphologies of the synthesized SOWSH@PCNC nanocomposites. Figure 1B shows that the $ZnSn(OH)_6$ precursor possesses cubic morphology with an average particle size of about 1 μm. After coating with polymer and reducing under the Ar/H_2 atmosphere, the initial cubic morphology was transformed to a large number of $SnO_2@Sn$ core−shell nanospheres, which are wrapped by the PCNC framework (Figures 1C and S1). Benefitting from the sacrifice and evaporation of Zn, abundant interspaces are formed to bear the volumetric changes of $SnO_2@Sn$ in lithiation/delithiation. However, in the presence of simple Super P carbon particles surrounding the $ZnSn(OH)_6$ composite without a polymer coating (Figure 1D), this unstable structure cannot effectively resist the growth of solid $SnO_2@Sn$ into larger particles, indicating that the nitrogen functional groups inhibit the
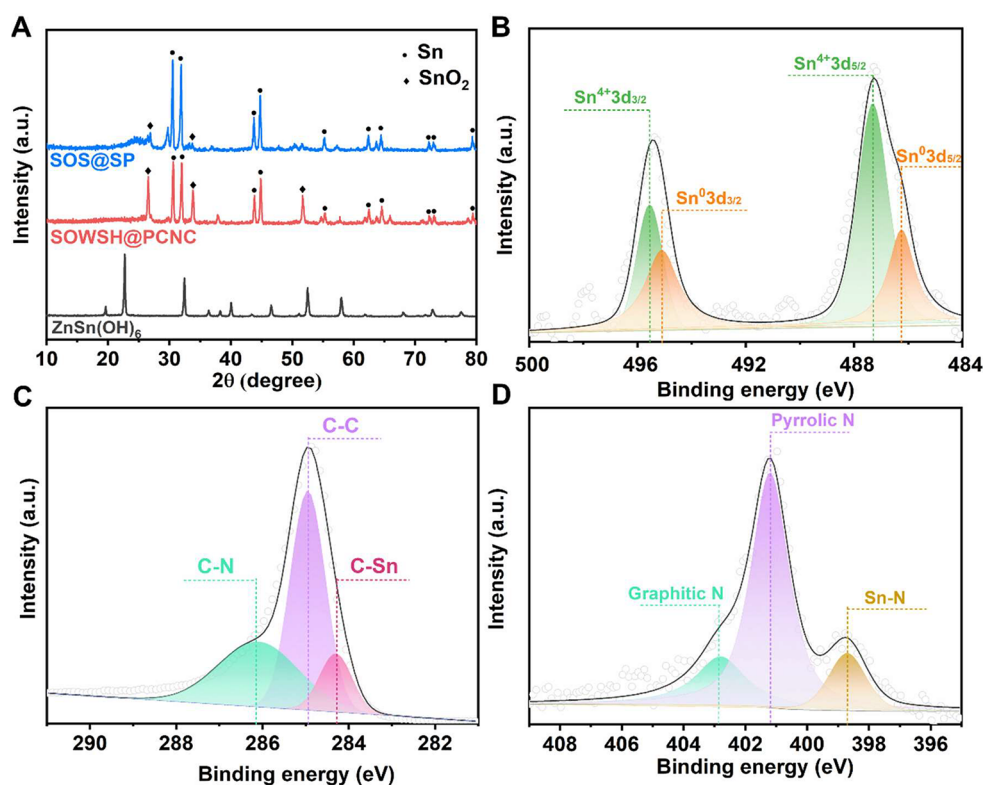
Figure 2. (A) XRD patterns of SOWSH@PCNC and SOS@SP nanocomposites. High-resolution XPS spectra of (B) Sn 3d, (C) C 1s, and (D) N 1s in the SOWSH@PCNC nanocomposite.

aggregation of SnO_2@Sn into nanosized particles. Meanwhile, the formed PCNC affords a more mechanically robust and flexible structure with affluent pores to facilitate the electrolyte infiltration and transport lithium ions throughout the interconnective structure. Elemental SEM mappings in Figures 1E and S2 show that all of the elemental Sn, N, O, and C are evenly scattered within the nanocomposite, demonstrating the uniform dispersion and successful embedding of the SnO_2@Sn nanoparticles within the PCNC without a large amount of aggregation. Furthermore, the TEM images in Figures 1F and S3 and S4 confirm the typical core–shell structure of the SnO_2@Sn nanoparticle with a size of around 300 nm, and it is well wrapped and covered by the porous PCNC layer highlighted in light green shadow (Figure 1F). The low- and high-resolution TEM images in Figures S3 and S4 further demonstrate the SnO_2 shell encapsulated Sn core construction and the heterojunction interfaces between Sn and SnO_2 within the nanosphere analogue. And the heterostructural SnO_2@Sn sites act as interfacial kinetic pumps to accelerate the Li^+ transfer. In the corresponding selected area electron diffraction (SAED) pattern (Figure 1G), many polycrystalline rings ascribed to the diffraction planes of (202) in SnO_2 and (312), (301), and (220) in Sn are presented, indicating the heterostructure of the core–shell SnO_2@Sn in the as-converted SOWSH@PCNC nanocomposites.

In the consecutive structural characterizations, two groups of diffraction peaks centered at 30.6, 32.0, and 44.9° as well as at 26.5, 33.8, and 51.7° are observed in the X-ray diffraction (XRD) patterns (Figure 2A), which should be precisely assigned to the (200), (101), and (211) crystal planes of pure Sn (JCPSD no. 86-2265) and the (110), (101), and (211) crystal planes of SnO_2 (JCPSD no. 71-0652), respectively. This indicates the full chemical transformation of the $ZnSn(OH)_6$

precursor into the SOWSH@PCNC materials. The contents of Sn and carbon in the SOWSH@PCNC composite can be calculated to be 60 and 40 wt % based on the thermal weight loss analysis. Due to the ultrathin layer of SnO_2 wrapping the outside of the Sn particle, the weight content of SnO_2 in the SOWSH@PCNC is negligible. The chemical bonding environment in the as-synthesized SOWSH@PCNC nanocomposite is further confirmed by X-ray photoelectron spectroscopy (XPS), as displayed in Figures 2B–D and S5. In the high-resolution Sn spectrum, two typical characteristic peaks located at 487.2 and 495.3 should be assigned to Sn^{4+} $3d_{5/2}$ and Sn^{4+} $3d_{3/2}$ for SnO_2 in Figure 2B, respectively.[30] The pair of peaks centered at 495.1 and 486.2 eV correspond to $3d_{5/2}$ and $3d_{3/2}$ of metallic Sn, respectively.[24] At the same time, the O 1s spectrum was deconvoluted into three components (Figure S5), which were attributed to the lattice oxygen of the Sn–O bond in SnO_2 (531.9 eV), defect oxygen or the surface oxygen ions (533.2 eV) derived from the heterojunction interfaces between the PCNC and SnO_2@Sn, and the surface-adsorbed oxygen species (534.7 eV).[51,52] Overall, the characteristic Sn–O bond and Sn^{4+} and Sn^0 peaks apparently demonstrate the existence of active Sn and SnO_2 in the SOWSH@PCNC nanocomposite with favorable chemical interactions. The C 1s spectrum of the SOWSH@PCNC was also examined (Figure 2C). It can be fitted into three peaks at 284.3, 284.9, and 286.1 eV, corresponding to C–Sn, C–C/C═C, and C–N species, respectively.[53] Among them, the C–Sn bond at 284.3 eV is attributed to the formation of heterojunction interfaces between the PCNC and SnO_2@Sn, which will remarkably modulate the electronic structure to speed up the electron/ion kinetics for fast lithiation. Moreover, it is widely accepted that more defect sites and vacancies derived from N doping can facilitate more lithium ion transformation accelerators. The
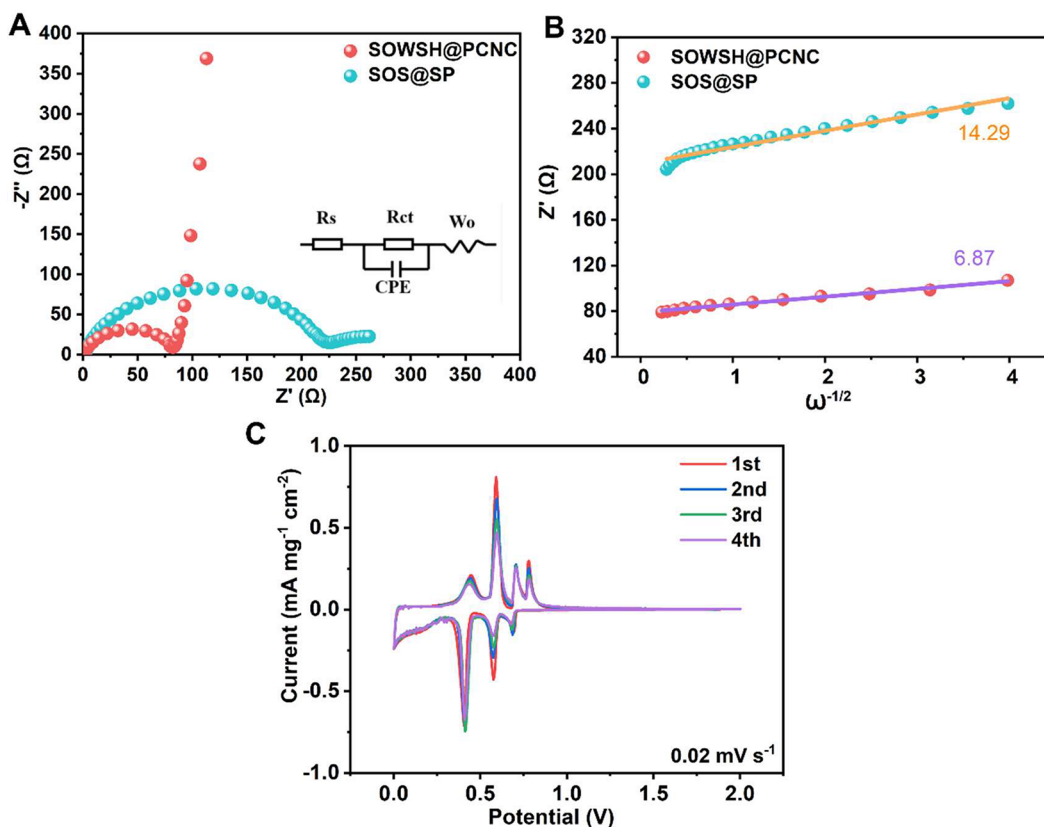
Figure 3. (A) Comparison of EIS between SOWSH@PCNC and SOS@SP electrodes and the corresponding equivalent circuit in the inset. (B) Corresponding linear relationship between the real part of the impedance (Z′) and the reciprocal exponential (−1/2) of the lower angular frequency (ω). (C) CV profiles of the SOWSH@PCNC electrode in the first four cycles after activation at 0.02 mV s⁻¹.

high-resolution N 1s spectrum in Figure 2D is deconvolved into three peaks located at 398.7, 401.2, and 402.9 eV, ascribing to the heterojunction Sn−N bond, pyrrolic N, and graphitic N species, respectively.[54−56]

The electrochemical performances of the cells based on the well-designed SOWSH@PCNC electrodes were comprehensively evaluated. Initially, the ion/electron conductivity and electrochemical reaction characteristics are tested by electrochemical impedance spectroscopy (EIS) and cyclic voltammetry (CV). As shown in Figure 3A, each EIS plot of the two cells typically presents a semicircle with a slope line, corresponding to the charge-transfer capability (Rct) at high frequency and the diffusion-controlled Warburg impedance (Wo) at low frequency, respectively. As we can see, the SOWSH@PCNC electrode possesses a remarkably decreased resistance compared to that of the controlled SOS@SP electrode (80 vs 219 Ω), indicating higher electron exchange between the active materials and the matrix. At the same time, the SOWSH@PCNC electrode exhibits much faster ion diffusion ability. According to the modified equations $D_{Li} = \frac{R^2 T^2}{2A^2 n^4 F^4 C^2 \sigma^2}$ and $Z' = B + \sigma\omega^{-1/2}$, the real part of the impedance (Z′) was plotted as a linear function of the reciprocal exponential (−1/2) of the lower angular frequency (ω), which can directly evaluate the diffusion coefficient (D_{Li}) of Li⁺.[57] As expected, a smaller slope (σ) for the SOWSH@PCNC electrode compared to the controlled one is achieved (6.87 vs 14.29) (Figure 3B), corresponding to the markedly enhanced D_{Li}, and the lithium ion diffusion coefficient in the SOWSH@PCNC is calculated to be 7.5 × 10⁻¹⁰. These fully evidence the much

improved electrochemical kinetics of the SnO₂@Sn electrode with a robust PCNC wrapping layer. To explore the specific electrochemical reaction process and the formation of the potential solid electrolyte interphase (SEI), cyclic voltammetry (CV) curves are monitored on the two electrodes, and the corresponding results are displayed in Figure 3C. In the initial cathodic sweep, the peaks at 0.695 and 0.573 V should be ascribed to the conversion reaction of SnO₂ to Li₂O and Sn (SnO₂ + 4Li⁺ + 4e⁻ → Sn + 2Li₂O) as well as the formation of SEI.[58] The major reductive peak located at 0.408 V is assigned to the multistep lithiation reactions of Sn that form the Li$_x$Sn alloy gradually (Sn + xLi⁺ + xe⁻ → Li$_x$Sn (0 ≤ x ≤ 4.4)). In the reverse delithiation process, a series of oxidation peaks from 0.442 to 0.779 V are ascribed to the dealloying process of the formed Li$_x$Sn to metallic Sn. In the subsequent cycles, the remarkable reduction peaks at 0.701 and 0.573 V suggest the formation of a stable LiF-Li₃N-rich SEI on the electrode surface to counter the volumetric change in the initial four cycles. At the same time, the CV curves recorded with the same scan rate display a good overlap tendency. However, the SOS@SP electrode reveals inferior reversibility and activity owing to the weak current density and worse overlap of the CV curves (Figure S6).

The rate capacity behaviors of the two electrodes are depicted in Figure 4A by varying the current densities from 100 to 1500 mA g⁻¹. The SOWSH@PCNC electrode initially delivers 1290, 847, 686, and 540 mA h g⁻¹ at current densities of 100, 200, 500, and 1500 mA g⁻¹, respectively, which demonstrates a small tendency in capacity fading with the increase in current density. After switching the current density
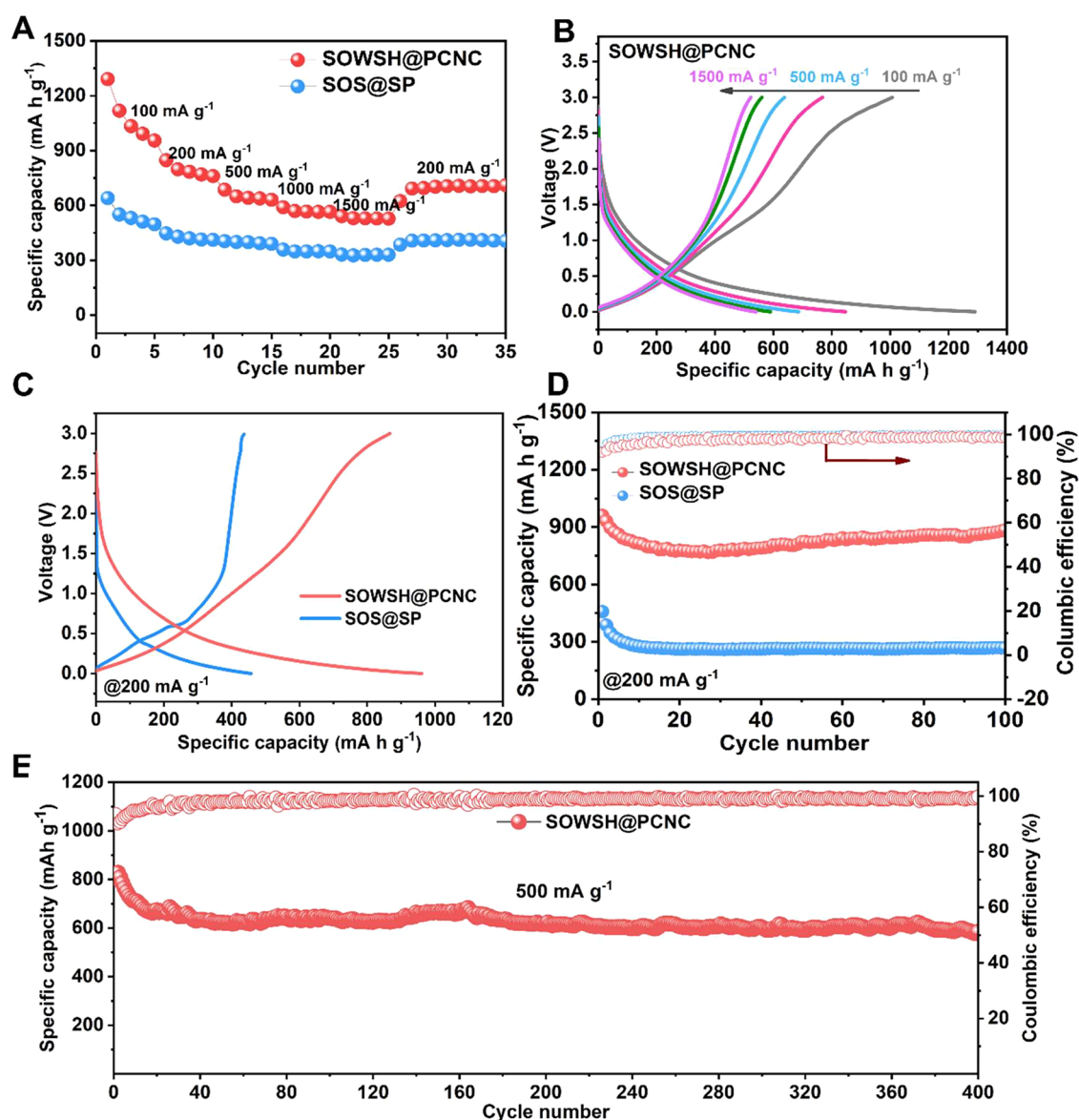
Figure 4. (A) Comparison of rate performances for the two electrodes at shifting current densities. (B) Voltage−capacity profiles of the SOWSH@PCNC electrode at shifting current densities. (C) Initial galvanostatic charge/discharge curves. (D) Cycling performances of SOWSH@PCNC and SOS@SP electrodes at a current density of 200 mA g^{-1}. (E) Long-cycle performance of the SOWSH@PCNC electrode at a current density of 500 mA g^{-1}.

back to 200 mA g^{-1}, the specific capacity could recover to 694 mA h g^{-1}, nearly 2 times higher than the commercial graphite anode (372 mA h g^{-1}),[27,29] corresponding to a recovery rate of 91.4% cycled at the same current density. In sharp contrast, the controlled SOS@SP electrode displays a much lower rate capacity when increasing the current densities. For example, the SOS@SP electrode merely contributes 331 mA h g^{-1} at 1500 mA g^{-1}, indicating the superiority of the cross-linked electronic network. The discharge and charge plateaus of the SOWSH@PCNC electrode at various current densities deliver gentle descending/rising and inapparent plateaus but are reversible even at a high current density of 1500 mA g^{-1} (Figure 4B), which is attributed to the continuous and quite near peak potential depicted in Figure 3C. However, the control electrode presents shortened and deformed plateaus with higher polarizations owing to sluggish kinetics (Figure S7).

The lithiation/delithiation profiles of the two electrodes at a constant current density of 200 mA g^{-1} are depicted in Figure 4C. It can be seen that the voltage profiles display multistep lithiation/delithiation plateaus for the active SnO$_2$@Sn, which remains in good agreement with the CV curves. More importantly, the SOWSH@PCNC electrode in Figure 4D delivers a higher specific capacity of 961 mA h g^{-1} with a significantly narrowed voltage gap than that of the controlled SOS@SP electrode (458 mA h g^{-1}). At the same time, the SOWSH@PCNC delivers a relatively low initial Coulombic efficiency (ICE) of 90%, which is ascribed to the inevitable formation of an SEI layer during the initial few cycles. In the subsequent cycles, the SOWSH@PCNC electrode maintains a stable cycling tendency and also a specific capacity of 885 mA h g^{-1} after 100 cycles, corresponding to a capacity retention rate of 92%. However, the SOS@SP electrode experiences a fast capacity decay and presents a much lower capacity. Also, as
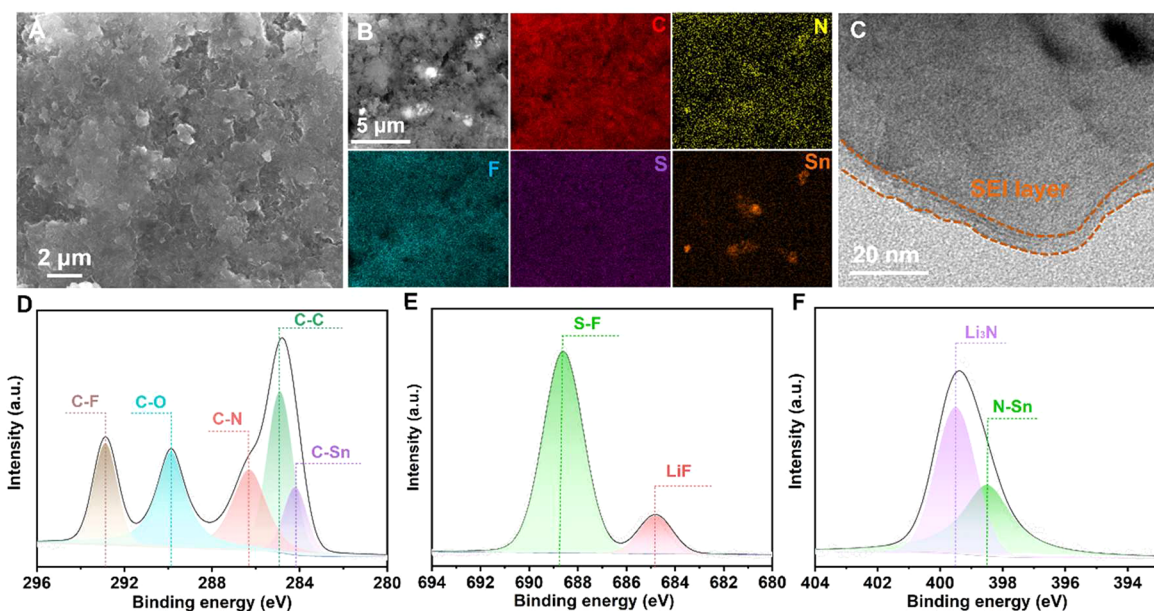
Figure 5. (A) SEM image and (B) EDS elemental mappings of C, N, F, S, and Sn conducted on the cycled SOWSH@PCNC electrode in a full lithiated state. (C) High-resolution TEM image of the cycled SOWSH@SP electrode evincing the existence of a SEI layer. High-resolution (D) C 1s, (E) F 1s, and (F) N 1s spectra of the delithiated SOWSH@PCNC electrode.

reflected in the EIS (Figure S8A), the SOWSH@PCNC electrode after 100 cycles experiences a significant decrease in charge transfer and lithium ion resistances compared to the SOS@SP electrode. An obviously reduced linear slope corresponds to the much-accelerated diffusion kinetics for the SOWSH@PCNC electrode after cycling, which could be attributed to the stable growth of an SEI layer derived from the active LiTFSI on the surface of the electrode (Figure S8B). Such a protective SEI layer would restrain the robustness of the SOWSH@PCNC structure and make the Li ion diffusion flux uniform across the interface to SnO_2@Sn particles, avoiding the focused large volumetric expansion to break the mechanical integrity of the electrode. Enhancing the current density to 500 mA g^{-1}, the SOWSH@PCNC electrode initially delivers a discharge capacity of 810 mA h g^{-1} and retains a reversible capacity of around 577 mA h g^{-1} after 400 cycles with a capacity decay rate of as low as 0.071% per cycle (Figure 4E). Moreover, the cell still delivers stable voltage profiles (Figure S9) with acceptable polarization potentials. For a better understanding of the merits of this SEI layer, the cycling performance of the cell with the commercial LiPF$_6$-based carbonate electrolyte (1 M LiPF$_6$ in ethylene carbonate and dimethyl carbonate (1:1 by volume)) is evaluated at a current density of 500 mA g^{-1}. In this case, the SOWSH@PCNC electrode merely had a lower discharge capacity of 660 mA h g^{-1} (Figure S10), much lower than 810 mA h g^{-1} for the LiTFSI-based ether electrolyte (Figure 4E). These results comprehensively indicate that the fabricated SOWSH@PCNC electrode is capable of providing more void to bear the volumetric changes so as to enhance the lithiation capacity. By a comparable analysis of the reported literature (Table S1), the much higher rate capacity and cycling stability with a small amount of electrolyte (15 μL mg^{-1}) further confirm the superiority of our strategy.

A stable SEI layer is another enhanced guarantee for the cycling stability of the electrode.[59−64] After activation, the SEI layer derived from a LiTFSI-type electrolyte is crucial to ensuring the robustness of the SOWSH@PCNC electrode within lithiation/delithiation. Then, SEM, TEM, and XPS characterizations have been conducted on the cycled electrode to confirm the surface morphologies and constituents of the cycled Sn electrode in the LiTFSI-based electrolyte (Figure 5). As revealed in the *ex situ* SEM of the cycled electrode (100 cycles at 200 mA g^{-1}), the SOWSH@PCNC electrode maintains its compactness and integrity without any fracture after cycling (Figure 5A). In either fully lithiated or delithiated states, the cycled SOWSH@PCNC electrodes exhibit a smooth surface rather than any obvious aggregation of the Sn nanoparticles resulting from structural collapse (Figures 5B and S11 and S12). At the same time, all of the elements in the lithiated/delithiated electrodes are uniformly distributed, including the Sn, C, and O elements originating from the initial SOWSH@PCNC nanocomposites and the characteristic elements of N, S, and F representing the reduced production of anion TFSI$^-$ in the formed LiF-Li$_3$N-rich SEI layer. Switching to the full charged state, a steady and robust SEI layer is bestowed due to the EDS mapping of the delithiated electrode displaying a uniform surface layer made up of these elements as well (Figure S12). Even when cycling for 400 cycles at a current of 500 mA g^{-1} (Figure S13), the SOWSH@PCNC electrode still affords a robust tolerance for the unified structure and a uniform SEI layer to bear long-term volumetric variations. However, many cracks resulting from volumetric expansion are observed on the surface of the SOS@SP electrode (Figure S14). Such a thin and consecutive film within several nanometers in the cycled SOWSH@PCNC electrode is further affirmed by the high-resolution TEM measurement in Figure 5C. Then, XPS analysis was carried out to seek the possible constituents of the beneficial SEI layer. The high-resolution C 1s spectrum is deconvoluted into five types of carbon-involved species (Figure 5D). Except for the C−Sn, C−C, and C−N bonds originating from the initial SOWSH@PCNC nanocomposites, the C−O species located at 289.8 eV is most probably assigned to the ether-based solvents (DME

and DOL). The peak positioned at 292.8 eV in relation to the C−F bond demonstrates the possible decomposition of a small amount of TFSI$^-$ during the electrochemical process. The refined F 1s spectrum in Figure 5E presents two characteristic peaks centered at 684.8 eV (LiF) and 688.6 eV (S−F), respectively. Both species demonstrate the reduction of the high reactivity of TFSI$^-$ on the Sn electrode surface with respect to the growth SEI layer. Meanwhile, different from the N 1s spectrum in initial SOWSH@PCNC nanocomposites, the cycled electrode mainly proves the existence of the N−Sn bond derived from N doping at the heterojunction interfaces and Li$_3$N species[65,66] that most likely relate to nitrogen-related matter reduced from the active TFSI$^-$ (Figure 5F). Overall, the atomic percentages of N and F contribute to 3.1 and 13.94 at. %, respectively, confirming the formation of the LiF-Li$_3$N-rich SEI layer again. As a supplementary proof, the deconvoluted peaks in the S 2p spectrum indicate the generation of SO$_x^{2-}$ species resulting from the reduction of the TFSI$^-$ group (Figure S15).

CONCLUSIONS

A heterostructural core−shell SnO$_2$@Sn nanoparticle embedded in a porous conductive N-doped carbon (SOWSH@ PCNC) is proposed and successfully synthesized via a facile self-sacrificial template method. The ZnSn(OH)$_6$ microcubes act as the sacrificial template for pore formation by evaporating Zn at high temperature, leaving hierarchical pores and providing abundant interspaces to buffer the volumetric change. Meanwhile, the wrapped polymer strengthens the mechanical properties of the electrode with the formation of porous conductive nitrogen-doped noncarbon (PCNC). Thanks to the synergistic robust LiF-Li$_3$N-rich SEI layer on the electrode, as comprehensively investigated by SEM, XPS, and TEM, the as-prepared SOWSH@PCNC delivers a high specific capacity of 961 mA h g^{-1} at 200 mA g^{-1} and retains a capacity of 885 mA h g^{-1} after 100 cycles, corresponding to a high retention rate of 92%. The electrode also shows excellent cycling stability with a low capacity decay rate of as low as 0.071% after 400 cycles at 500 mA g^{-1}. These results shed light on the bright future of developing high-capacity Sn-based anodes for high-energy-density lithium ion batteries.

AUTHOR INFORMATION

Corresponding Authors

Jing Zhang − *School of Materials Science and Engineering, Xi'an University of Technology, Xi'an, Shaanxi 710048, China*; Email: zhangjing2020@xaut.edu.cn

Yonglan Xi − *Institute of Agricultural Resources and Environment, Institute of Animal Science, Jiangsu Academy of Agricultural Sciences, Nanjing 210014, China*; Email: yonglanxi@jaas.ac.cn

Fangmin Ye − *Department of Physics, Zhejiang Sci-Tech University, Hangzhou 310018, China*; orcid.org/0000-0001-6595-0881; Email: fmye2013@sinano.ac.cn

Hongzhen Lin − *i-Lab & CAS Key Laboratory of Nanophotonic Materials and Devices, Suzhou Institute of Nano-tech and Nano-bionics, Chinese Academy of Sciences, Suzhou 215123, China*; Email: hzlin2010@sinano.ac.cn

Jian Wang − *i-Lab & CAS Key Laboratory of Nanophotonic Materials and Devices, Suzhou Institute of Nano-tech and Nano-bionics, Chinese Academy of Sciences, Suzhou 215123, China; Helmholtz Institute Ulm (HIU), Ulm D89081, Germany*; orcid.org/0000-0002-7945-0826; Email: wangjian2014@sinano.ac.cn, jian.wang@kit.edu

Authors

Bo Deng − *Advanced Material Analysis and Test Center, Xi'an University of Technology, Xi'an, Shaanxi 710048, China; School of Materials Science and Engineering, Xi'an University of Technology, Xi'an, Shaanxi 710048, China*

Rong He − *School of Materials Science and Engineering, Xi'an University of Technology, Xi'an, Shaanxi 710048, China*

Caiyin You − *School of Materials Science and Engineering, Xi'an University of Technology, Xi'an, Shaanxi 710048, China*

Qingbo Xiao − *Institute of Agricultural Resources and Environment, Institute of Animal Science, Jiangsu Academy of Agricultural Sciences, Nanjing 210014, China*; orcid.org/0000-0002-1758-8512

Yongzheng Zhang − *State Key Laboratory of Chemical Engineering, East China University of Science and Technology, Shanghai 200237, China*

Haitao Liu − *Laboratory of Computational Physics, Institute of Applied Physics and Computational Mathematics, Beijing 100088, China*; orcid.org/0000-0002-1453-5431

Meinan Liu − *i-Lab & CAS Key Laboratory of Nanophotonic Materials and Devices, Suzhou Institute of Nano-tech and Nano-bionics, Chinese Academy of Sciences, Suzhou 215123, China*; orcid.org/0000-0003-2552-1091

Notes

The authors declare no competing financial interest.

REFERENCES

(1) Wang, J.; Li, L.; Hu, H.; Hu, H.; Guan, Q.; Huang, M.; Jia, L.; Adenusi, H.; Tian, K. V.; Zhang, J.; Passerini, S.; Lin, H. Toward

Dendrite-Free Metallic Lithium Anodes: From Structural Design to Optimal Electrochemical Diffusion Kinetics. *ACS Nano* **2022**, *16*, 17729−17760.

(2) Zhang, J.; You, C.; Lin, H.; Wang, J. Electrochemical Kinetics Modulators in Lithium Sulfur Batteries: From Defect-Rich Catalysts to Single Atomic Catalysts. *Energy Environ. Mater.* **2022**, *5*, 731−750.

(3) Wang, Y.; Zhang, R.; Chen, J.; Wu, H.; Lu, S.; Wang, K.; Li, H.; Harris, C. J.; Xi, K.; Kumar, R. V.; Ding, S. Enhancing Catalytic Activity of Titanium Oxide in Lithium-Sulfur Batteries by Band Engineering. *Adv. Energy Mater.* **2019**, *9*, 1900953.

(4) Zhang, P.; Li, Y.; Gao, M.; Yang, S.; Wang, M.; Liu, Z.; Guo, K.; Wang, F.; Lu, X. Biomimetic Platinum Forest Enables 3D Micro-Supercapacitors with Enhanced Areal Performance. *Chem. Eng. J.* **2023**, *454*, 140357.

(5) Zhang, J.; He, R.; Jia, L.; You, C.; Zhang, Y.; Liu, M.; Tian, N.; Lin, H.; Wang, J. Strategies for Realizing Rechargeable High Volumetric Energy Density Conversion-Based Aluminum-Sulfur Batteries. *Adv. Funct. Mater.* **2023**, 2305674.

(6) Li, J.; Zhang, Q.; Zhang, J.; Wu, N.; Liu, G.; Chen, H.; Yuan, C.; Liu, X. Optimizing Electronic Structure of Porous Ni/MoO_2 Heterostructure to Boost Alkaline Hydrogen Evolution Reaction. *J. Colloid Interface Sci.* **2022**, *627*, 862−871.

(7) Zhang, J.; Jia, L.; Lin, H.; Wang, J. Advances and Prospects of 2D Graphene-Based Materials/Hybrids for Lithium Metal-Sulfur Full Battery: From Intrinsic Property to Catalysis Modification. *Adv. Energy Sustainability Res.* **2022**, *3*, 2100187.

(8) Jeong, J.; Lee, J.; Kim, J.; Chun, J.; Kang, D.; Han, S. M.; Jo, C.; Lee, J. A Biopolymer-Based Functional Separator for Stable Li Metal Batteries with an Additive-Free Commercial Electrolyte. *J. Mater. Chem. A* **2021**, *9*, 7774−7781.

(9) Kim, J.; Park, J.; Lee, J.; Lim, W. G.; Jo, C.; Lee, J. Biomass-Derived P, N Self-Doped Hard Carbon as Bifunctional Oxygen Electrocatalyst and Anode Material for Seawater Batteries. *Adv. Funct. Mater.* **2021**, *31*, 2010882.

(10) Deng, P.; Yang, J.; Li, S.; Fan, T. E.; Wu, H. H.; Mou, Y.; Huang, H.; Zhang, Q.; Peng, D. L.; Qu, B. High Initial Reversible Capacity and Long Life of Ternary SnO_2-Co-carbon Nanocomposite Anodes for Lithium-Ion Batteries. *Nano-micro Lett.* **2019**, *11*, 18.

(11) Yang, Z.; Wu, H. H.; Zheng, Z.; Cheng, Y.; Li, P.; Zhang, Q.; Wang, M. S. Tin Nanoparticles Encapsulated Carbon Nanoboxes as High-Performance Anode for Lithium-Ion Batteries. *Front. Chem.* **2018**, *6*, 533.

(12) Wan, M.; Kang, S.; Wang, L.; Lee, H. W.; Zheng, G. W.; Cui, Y.; Sun, Y. Mechanical Rolling Formation of Interpenetrated Lithium Metal/Lithium Tin Alloy Foil for Ultrahigh-Rate Battery Anode. *Nat. Commun.* **2020**, *11*, 829.

(13) Wang, J.; Zhang, J.; Duan, S.; Li, T.; Jia, L.; Liu, H.; Li, L.; Cheng, S.; Hu, H.; Huang, M.; Hu, H.; Zhang, S.; Xiao, Q.; Lin, H. Interfacial Lithium-Nitrogen Bond Catalyzes Sulfide Oxidation Reactions in High-Loading Li_2S Cathode. *Chem. Eng. J.* **2022**, *429*, 132352.

(14) Wang, J.; Jia, L.; Duan, S.; Liu, H.; Xiao, Q.; Li, T.; Fan, H.; Feng, K.; Yang, J.; Wang, Q.; Liu, M.; Zhong, J.; Duan, W.; Lin, H.; Zhang, Y. Single Atomic Cobalt Catalyst Significantly Accelerates Lithium Ion Diffusion in High Mass Loading Li_2S Cathode. *Energy Storage Mater.* **2020**, *28*, 375−382.

(15) Wang, B.; Yuan, W.; Zhang, X.; Xiang, M.; Zhang, Y.; Liu, H.; Wu, H. Sandwiching Defect-Rich $TiO_{2-\delta}$ Nanocrystals into a Three-Dimensional Flexible Conformal Carbon Hybrid Matrix for Long-Cycling and High-Rate Li/Na-Ion Batteries. *Inorg. Chem.* **2019**, *58*, 8841−8853.

(16) Wu, C.; Zhu, G.; Wang, Q.; Wu, M.; Zhang, H. Sn-Based Nanomaterials: From Composition aand Structural Design to Their Electrochemical Performances ffor Li-And Na-Ion Batteries. *Energy Storage Mater.* **2021**, *43*, 430−462.

(17) Xin, F.; Whittingham, M. S. Challenges and Development of Tin-Based Anode with High Volumetric Capacity for Li-Ion Batteries. *Electrochem. Energy Rev.* **2020**, *3*, 643−655.

(18) Chen, T.; Hu, Y.; Cheng, B.; Chen, R.; Lv, H.; Ma, L.; Zhu, G.; Wang, Y.; Yan, C.; Tie, Z.; Jin, Z.; Liu, J. Multi-Yolk-Shell Copper Oxide@Carbon Octahedra as High-Stability Anodes for Lithium-Ion Batteries. *Nano Energy* **2016**, *20*, 305−314.

(19) Zhu, G.; Wang, L.; Lin, H.; Ma, L.; Zhao, P.; Hu, Y.; Chen, T.; Chen, R.; Wang, Y.; Tie, Z.; Liu, J.; Jin, Z. Walnut-Like Multicore-Shell MnO Encapsulated Nitrogen-Rich Carbon Nanocapsules as Anode Material for Long-Cycling and Soft-Packed Lithium-Ion Batteries. *Adv. Funct. Mater.* **2018**, *28*, 1800003.

(20) Xie, J.; Sun, L.; Liu, Y.; Xi, X.; Chen, R.; Jin, Z. $Siox$/C-Ag Nanosheets Derived from Zintl Phase $Casi_2$ Via a Facile Redox Reaction for High Performance Lithium Storage. *Nano Res.* **2022**, *15*, 395−400.

(21) Li, W.; Sun, X.; Yu, Y. Si-, Ge-, Sn-Based Anode Materials for Lithium-Ion Batteries: From Structure Design to Electrochemical Performance. *Small Methods* **2017**, *1*, 1600037.

(22) Ying, H.; Han, W. Q. Metallic Sn-Based Anode Materials: Application in High-Performance Lithium-Ion and Sodium-Ion Batteries. *Adv. Sci.(Weinh)* **2017**, *4*, 1700298.

(23) Shi, H.; Fang, Z.; Zhang, X.; Li, F.; Tang, Y.; Zhou, Y.; Wu, P.; Yu, G. Double-Network Nanostructured Hydrogel-Derived Ultrafine Sn-Fe Alloy in Three-Dimensional Carbon Framework for Enhanced Lithium Storage. *Nano Lett.* **2018**, *18*, 3193−3198.

(24) Nowak, A. P.; Trzciński, K.; Szkoda, M.; Trykowski, G.; Gazda, M.; Karczewski, J.; Łapiński, M.; Maskowicz, D.; Sawczak, M.; Lisowska-Oleksiak, A. Nano Tin/Tin Oxide Attached onto Graphene Oxide Skeleton as a Fluorine Free Anode Material for Lithium-Ion Batteries. *Inorg. Chem.* **2020**, *59*, 4150−4159.

(25) Zhou, J.; You, Y.; Lian, X.; Shi, Q.; Liu, Y.; Yang, X.; Bachmatiuk, A.; Liu, L.; Sun, J.; Yang, R.; Choi, J.-H.; Rümmeli, M. H. Toward Stable Lithium-Ion Batteries: Accelerating the Transfer and Alloying Reactions of Sn-Based Anodes via Coordination Atom Regulation and Carbon Hybridization. *J. Power Sources* **2022**, *519*, 230778.

(26) Cheng, F.; Li, W.-C.; Zhu, J.-N.; Zhang, W.-P.; Lu, A.-H. Designed Synthesis of Nitrogen-Rich Carbon Wrapped Sn Nano-particles Hybrid Anode via In-Situ Growth of Crystalline ZIF-8 on a Binary Metal Oxide. *Nano Energy* **2016**, *19*, 486−494.

(27) Wang, G.; Aubin, M.; Mehta, A.; Tian, H.; Chang, J.; Kushima, A.; Sohn, Y.; Yang, Y. Stabilization of Sn Anode through Structural Reconstruction of a Cu-Sn Intermetallic Coating Layer. *Adv. Mater.* **2020**, *32*, 2003684.

(28) Hassan, F. M.; Chen, Z.; Yu, A.; Chen, Z.; Xiao, X. Sn/SnO_2 Embedded in Mesoporous Carbon Nanocomposites as Negative Electrode for Lithium Ion Batteries. *Electrochim. Acta* **2013**, *87*, 844−852.

(29) Wang, J.; Yang, J.; Xiao, Q.; Jia, L.; Lin, H.; Zhang, Y. Hierarchical Sulfur-Doped Graphene Foam Embedded with Sn Nanoparticles for Superior Lithium Storage in LiFSI-Based Electrolyte. *ACS Appl. Mater. Interfaces* **2019**, *11*, 30500−30507.

(30) Li, R.; Nie, S.; Miao, C.; Xin, Y.; Mou, H.; Xu, G.; Xiao, W. Heterostructural Sn/Sno_2 Microcube Powders Coated by a Nitrogen-Doped Carbon Layer as Good-Performance Anode Materials for Lithium Ion Batteries. *J. Colloid Interface Sci.* **2022**, *606*, 1042−1054.

(31) Du, F. H.; Liu, Y. S.; Long, J.; Zhu, Q. C.; Wang, K. X.; Wei, X.; Chen, J. S. Incorporation of Heterostructured Sn/SnO Nanoparticles in Crumpled Nitrogen-Doped Graphene Nanosheets for Application as Anodes in Lithium-Ion Batteries. *Chem. Commun. (Camb)* **2014**, *50*, 9961.

(32) Lee, J. I.; Song, J.; Cha, Y.; Fu, S.; Zhu, C.; Li, X.; Lin, Y.; Song, M.-K. Multifunctional SnO_2/3D Graphene Hybrid Materials for Sodium-Ion and Lithium-Ion Batteries with Excellent Rate Capability and Long Cycle Life. *Nano Res.* **2017**, *10*, 4398−4414.

(33) Guo, Y.; Zeng, X.; Zhang, Y.; Dai, Z.; Fan, H.; Huang, Y.; Zhang, W.; Zhang, H.; Lu, J.; Huo, F.; Yan, Q. Sn Nanoparticles Encapsulated in 3D Nanoporous Carbon Derived from a Metal-Organic Framework for Anode Material in Lithium-Ion Batteries. *ACS Appl. Mater. Interfaces* **2017**, *9*, 17172−17177.

(34) Sun, L.; Si, H.; Zhang, Y.; Shi, Y.; Wang, K.; Liu, J.; Zhang, Y. Sn-SnO₂ Hybrid Nanoclusters Embedded in Carbon Nanotubes with Enhanced Electrochemical Performance for Advanced Lithium Ion Batteries. *J. Power Sources* **2019**, *415*, 126−135.

(35) Zhang, H.; Huang, X.; Noonan, O.; Zhou, L.; Yu, C. Tailored Yolk-Shell Sn@C Nanoboxes for High-Performance Lithium Storage. *Adv. Funct. Mater.* **2017**, *27*, 1606023.

(36) Mo, R.; Tan, X.; Li, F.; Tao, R.; Xu, J.; Kong, D.; Wang, Z.; Xu, B.; Wang, X.; Wang, C.; Li, J.; Peng, Y.; Lu, Y. Tin-Graphene Tubes as Anodes for Lithium-Ion Batteries with High Volumetric and Gravimetric Energy Densities. *Nat. Commun.* **2020**, *11*, 1374.

(37) Li, Z.; Yin, Q.; Hu, W.; Zhang, J.; Guo, J.; Chen, J.; Sun, T.; Du, C.; Shu, J.; Yu, L.; Zhang, J. Tin/tin Antimonide Alloy Nanoparticles Embedded in Electrospun Porous Carbon Fibers as Anode Materials for Lithium-Ion Batteries. *J. Mater. Sci.* **2019**, *54*, 9025−9033.

(38) Sadan, M. K.; Kim, H.; Kim, C.; Cho, G.-B.; Cho, K.-K.; Ahn, J.-H.; Ahn, H. J. Ultra-long Cycle Life of Flexible Sn Anode Using DME Electrolyte. *J. Alloys Compd.* **2021**, *871*, 159549.

(39) Xu, Z.; Yang, J.; Zhang, T.; Sun, L.; Nuli, Y.; Wang, J.; Hirano, S. i. Stable Na Metal Anode Enabled by a Reinforced Multistructural SEI Layer. *Adv. Funct. Mater.* **2019**, 1901924.

(40) Wang, D.; Luan, C.; Zhang, W.; Liu, X.; Sun, L.; Liang, Q.; Qin, T.; Zhao, Z.; Zhou, Y.; Wang, P.; Zheng, W. Zipper-Inspired SEI Film for Remarkably Enhancing the Stability of Li Metal Anode via Nucleation Barriers Controlled Weaving of Lithium Pits. *Adv. Energy Mater.* **2018**, *8*, 1800650.

(41) Wang, J.; Jia, L.; Zhong, J.; Xiao, Q.; Wang, C.; Zang, K.; Liu, H.; Zheng, H.; Luo, J.; Yang, J.; Fan, H.; Duan, W.; Wu, Y.; Lin, H.; Zhang, Y. Single-Atom Catalyst Boosts Electrochemical Conversion Reactions in Batteries. *Energy Storage Mater.* **2019**, *18*, 246−252.

(42) Eom, K.; Jung, J.; Lee, J. T.; Lair, V.; Joshi, T.; Lee, S. W.; Lin, Z.; Fuller, T. F. Improved Stability of Nano-Sn Electrode with High-Quality Nano-SEI Formation for Lithium Ion Battery. *Nano Energy* **2015**, *12*, 314−321.

(43) Seo, D. M.; Nguyen, C. C.; Young, B. T.; Heskett, D. R.; Woicik, J. C.; Lucht, B. L. Characterizing Solid Electrolyte Interphase on Sn Anode in Lithium Ion Battery. *J. Electrochem. Soc.* **2015**, *162*, A7091−A7095.

(44) Adenusi, H.; Chass, G. A.; Passerini, S.; Tian, K. V.; Chen, G. Lithium Batteries and the Solid Electrolyte Interphase (SEI)-Progress and Outlook. *Adv. Energy Mater.* **2023**, *13*, 2203307.

(45) Wang, J.; Cheng, S.; Li, L.; Jia, L.; Wu, J.; Li, X.; Guan, Q.; Hu, H.; Zhang, J.; Lin, H. Robust Interfacial Engineering Construction to Alleviate Polysulfide Shuttling in Metal Sulfide Electrodes for Achieving Fast-Charge High-Capacity Lithium Storages. *Chem. Eng. J.* **2022**, *446*, 137291.

(46) Wang, J.; Hu, H.; Duan, S.; Xiao, Q.; Zhang, J.; Liu, H.; Kang, Q.; Jia, L.; Yang, J.; Xu, W.; Fei, H.; Cheng, S.; Li, L.; Liu, M.; Lin, H.; Zhang, Y. Construction of Moisture-Stable Lithium Diffusion-Controlling Layer toward High Performance Dendrite-Free Lithium Anode. *Adv. Funct. Mater.* **2022**, *32*, 2110468.

(47) Wang, J.; Yang, J.; Xiao, Q.; Zhang, J.; Li, T.; Jia, L.; Wang, Z.; Cheng, S.; Li, L.; Liu, M.; Liu, H.; Lin, H.; Zhang, Y. In Situ Self-Assembly of Ordered Organic/Inorganic Dua-Layered Interphase for Achieving Long-Life Dendrite-Free Li Metal Anodes in LiFSI-Based Electrolyte. *Adv. Funct. Mater.* **2021**, *31*, 2007434.

(48) Zhang, H.; Wang, D.; Shen, C. In-situ EC-AFM And Ex-Situ XPS Characterization to Investigate the Mechanism of SEI Formation in Highly Concentrated Aqueous Electrolyte for Li-Ion Batteries. *Appl. Surf. Sci.* **2020**, *507*, 145059.

(49) Wang, J.; Hu, H.; Zhang, J.; Li, L.; Jia, L.; Guan, Q.; Hu, H.; Liu, H.; Jia, Y.; Zhuang, Q.; Cheng, S.; Huang, M.; Lin, H. Hydrophobic Lithium Diffusion-Accelerating Layers Enables Long-Life Moisture-Resistant Metallic Lithium Anodes in Practical Harsh Environments. *Energy Storage Mater.* **2022**, *52*, 210−219.

(50) Fan, B.; Liu, J.; Xu, Y.; Tang, Q.; Zhang, Y.; Chen, X.; Hu, A. A Facile Strategy Towards High Capacity and Stable Sn Anodes for Li-Ion Battery: Dual-Confinement via Sn@SnO₂ Core-Shell Nano-particles Embedded in 3D Graphitized Porous Carbon Network. *J. Alloys Compd.* **2021**, *857*, 157920.

(51) Zhang, J.; He, R.; Zhuang, Q.; Ma, X.; You, C.; Hao, Q.; Li, L.; Cheng, S.; Lei, L.; Deng, B.; Li, X.; Lin, H.; Wang, J. Tuning 4f-Center Electron Structure by Schottky Defects for Catalyzing Li Diffusion to Achieve Long-Term Dendrite-Free Lithium Metal Battery. *Adv. Sci. (Weinh)* **2022**, *9*, 2202244.

(52) Jiang, M.; Fu, C.; Yang, J.; Liu, Q.; Zhang, J.; Sun, B. Defect-Engineered MnO₂ Enhancing Oxygen Reduction Reaction for High Performance Al-Air Batteries. *Energy Storage Mater.* **2019**, *18*, 34−42.

(53) Zhang, J.; Duan, S.; You, C.; Wang, J.; Liu, H.; Guo, S.; Zhang, W.; Yang, R. In-Situ Grown Tungsten Carbide Nanoparticles on Nanocarbon as an Electrocatalyst to Promote the Redox Reaction Kinetics of High-Mass Loading Sulfur Cathode for High Volumetric Performance. *J. Mater. Chem. A* **2020**, *8*, 22240−22250.

(54) Zhang, J.; You, C.; Wang, J.; Xu, H.; Zhu, C.; Guo, S.; Zhang, W.; Yang, R.; Xu, Y. Confinement of Sulfur Species into Heteroatom-Doped, Porous Carbon Container for High Areal Capacity Cathode. *Chem. Eng. J.* **2019**, *368*, 340−349.

(55) Wang, J.; Cheng, S.; Li, W.; Jia, L.; Xiao, Q.; Hou, Y.; Zheng, Z.; Li, H.; Zhang, S.; Zhou, L.; Liu, M.; Lin, H.; Zhang, Y. Robust Electrical "Highway" Network for High Mass Loading Sulfur Cathode. *Nano Energy* **2017**, *40*, 390−398.

(56) Zhang, J.; You, C.; Zhang, W.; Wang, J.; Guo, S.; Yang, R.; Xu, Y. Conductive Bridging Effect of TiN Nanoparticles on the Electrochemical Performance of TiN@CNT-S Composite Cathode. *Electrochim. Acta* **2017**, *250*, 159−166.

(57) Wang, Q.; Tian, N.; Xu, K.; Han, L.; Zhang, J.; Zhang, W.; Guo, S.; You, C. A Facile Method of Improving the High Rate Cycling Performance of Lini₁/₃Co₁/₃Mn₁/₃O₂ Cathode Material. *J. Alloys Compd.* **2016**, *686*, 267−272.

(58) Zhang, L.; Zhao, K.; Sun, C.; Yu, R.; Zhuang, Z.; Li, J.; Xu, W.; Wang, C.; Xu, W.; Mai, L. Compact Sn/SnO₂ Microspheres with Gradient Composition for High Volumetric Lithium Storage. *Energy Storage Mater.* **2020**, *25*, 376−381.

(59) Tu, Z.; Choudhury, S.; Zachman, M. J.; Wei, S.; Zhang, K.; Kourkoutis, L. F.; Archer, L. A. Designing Artificial Solid-Electrolyte Interphases for Single-Ion and High-Efficiency Transport in Batteries. *Joule* **2017**, *1*, 394−406.

(60) Park, K. H.; Bai, Q.; Kim, D. H.; Oh, D. Y.; Zhu, Y.; Mo, Y.; Jung, Y. S. Design Strategies, Practical Considerations, and New Solution Processes of Sulfide Solid Electrolytes for All-Solid-State Batteries. *Adv. Energy Mater.* **2018**, *8* (18), 1800035.

(61) Xu, Y.; Dong, K.; Jie, Y.; Adelhelm, P.; Chen, Y.; Xu, L.; Yu, P.; Kim, J.; Kochovski, Z.; Yu, Z.; Li, W.; LeBeau, J.; Shao-Horn, Y.; Cao, R.; Jiao, S.; Cheng, T.; Manke, I.; Lu, Y. Promoting Mechanistic Understanding of Lithium Deposition and Solid-Electrolyte Inter-phase (SEI) Formation Using Advanced Characterization and Simulation Methods: Recent Progress, Limitations, and Future Perspectives. *Adv. Energy Mater.* **2022**, *12*, 2200398.

(62) Huang, K.; Bi, S.; Kurt, B.; Xu, C.; Wu, L.; Li, Z.; Feng, G.; Zhang, X. Regulation of SEI Formation by Anion Receptors to Achieve Ultra-Stable Lithium-Metal Batteries. *Angew. Chem., Int. Ed. Engl.* **2021**, *60*, 19232−19240.

(63) Wang, J.; Zhang, J.; Duan, S.; Jia, L.; Xiao, Q.; Liu, H.; Hu, H.; Cheng, S.; Zhang, Z.; Li, L.; Duan, W.; Zhang, Y.; Lin, H. Lithium Atom Surface Diffusion and Delocalized Deposition Propelled by Atomic Metal Catalyst toward Ultrahigh-Capacity Dendrite-Free Lithium Anode. *Nano Lett.* **2022**, *22*, 8008−8017.

(64) Wang, J.; Zhang, J.; Cheng, S.; Yang, J.; Xi, Y.; Hou, X.; Xiao, Q.; Lin, H. Long-Life Dendrite-Free Lithium Metal Electrode Achieved by Constructing a Single Metal Atom Anchored in a Diffusion Modulator Layer. *Nano Lett.* **2021**, *21*, 3245−3253.

(65) Kim, M. S.; Zhang, Z.; Wang, J.; Oyakhire, S. T.; Kim, S. C.; Yu, Z.; Chen, Y.; Boyle, D. T.; Ye, Y.; Huang, Z.; Zhang, W.; Xu, R.; Sayavong, P.; Bent, S. F.; Qin, J.; Bao, Z.; Cui, Y. Revealing the Multifunctions of Li₃N in the Suspension Electrolyte for Lithium Metal Batteries. *ACS Nano* **2023**, *17*, 3168−3180.

(66) Liu, J.; Wu, M.; Li, X.; Wu, D.; Wang, H.; Huang, J.; Ma, J. Amide-Functional, Li_3N/LiF-Rich Heterostructured Electrode Electrolyte Interphases for 4.6 V Li‖$LiCoO_2$ Batteries. *Adv. Energy Mater.* **2023**, *13*, 202300084.